Experimental Radiation Investigations

18

Lukas Pörtner, Philipp Graeser, Jeanette Gorewoda,
Matthias Koch, Martin Schiemann, Viktor Scherer
and Reinhold Kneer

Contents

18.1 Introduction 500
18.2 Emissivity of Solid Fuel Particles 501
    18.2.1 State of Research 501
    18.2.2 Emissivity Definition 501
    18.2.3 Experimental Setups 502
    18.2.4 Methods 504
    18.2.5 Results 506
18.3 Normal Spectral Radiative Emittance of Ash Layers Under Oxy-Fuel Conditions 510
    18.3.1 Experimental Setup 512
    18.3.2 Methods 513
    18.3.3 Results 513
18.4 Scattering Experiment 515

L. Pörtner (✉) · P. Graeser · J. Gorewoda · M. Schiemann · V. Scherer
Department of Energy Plant Technology, Ruhr-Universität Bochum, Bochum, Germany
e-mail: poertner@leat.rub.de

P. Graeser
e-mail: graeser@leat.rub.de

J. Gorewoda
e-mail: gorewoda@leat.rub.de

M. Schiemann
e-mail: schiemann@leat.rub.de

V. Scherer
e-mail: scherer@leat.rub.de

M. Koch · R. Kneer
Institute of Heat and Mass Transfer, RWTH Aachen University, Aachen, Germany
e-mail: koch@wsa.rwth-aachen.de

R. Kneer
e-mail: kneer@wsa.rwth-aachen.de

R. Kneer et al. (eds.), *Clean Energy Conversion*,
https://doi.org/10.1007/978-3-031-98956-8_18

18.4.1 Setup A: Acoustic Levtiator ... 515
18.4.2 Setup B: Flat Flame Burner ... 516
18.4.3 Assessment of the Phase Function ... 517
18.4.4 Resulting Complex Index of Refraction ... 518
18.5 Conclusion ... 519
References ... 520

Abstract

The experimental investigation of radiation in large combustion chambers is challenging due to the harsh environment and various radiation effects. This chapter presents experimental findings from several laboratory-scale studies that examined these effects separately. One goal was to determine the emissivity of the solid fuels and of ash utilising two setups: (1) observing a particle streak in a laminar flow reactor (LFR) and (2) studying laser-ignited fuel particles. The emissivity of both investigated solid fuels (Colombian bituminous coal and walnut shells) decreased with increasing temperature and progressing conversion, where mineral content has also an influence. For particles at higher levels of conversion, a final increase in emissivity was noticed. A spectroscopic experiment examined the emissivity of typical ash components and their mixtures. Carbonates and sulphates exhibited characteristic temperature- and wavelength-dependent emission trends, with specific emission bands attributed to CO_3 and S–O functional groups. Another goal was to determine the index of refraction of the solid fuels experimentally. It was measured at room temperature and for burning particles applying inverse Mie-theory.

18.1 Introduction

In pulverised fuel combustion chambers, radiative heat transfer is one of the major heat transfer mechanisms. Especially in large systems, the influence of radiation exceeds the heat transfer contributions of convection and conduction. Considering all possible radiation sources in such a chamber, the radiation can be separated into three main parts. These parts are particle radiation, gas radiation, and the radiation emitted by the chamber walls. The main source of thermal radiation in combustion systems are solid materials, namely the fuel particles and the chamber walls. Consequently, the individual solid fuel particle and wall material radiative parameters have a decisive influence on the behaviour of the combustion process. In addition to the emission of radiation from varying sources, also the interaction of solid materials with thermal radiation inside the chamber needs to be considered. The interaction of single fuel particles with thermal radiation is of special interest, as the typical particle sizes lead to complex radiation scattering effects.

18.2 Emissivity of Solid Fuel Particles

18.2.1 State of Research

From the study by Chen et al. [1] it is known that the contribution of particle radiation to the overall radiation in an oxy-fuel combustion system can rise to 70%. This confirms the high interest in a well-defined emissivity of the applied single fuel particles visible in the series of studies which aimed for this parameter.

First, the influence of iron oxide Fe_2O_3 and Fe_3O_4 on the emissivity of fuels was investigated and proven by Boow and Goard [2]. Following, this result was confirmed by Wall et al. [3] and Brewster and Kunitomo [4]. For Fe_2O_3, these results were extended by the results of Greffrath et al. [5], who showed a dependence of fuel ash emissivity from the ash's iron content.

With the known influence of different fuel compositions, Baxter et al. [6] measured the emissivity of single coal particle layers of various degrees of carbonisation at temperatures below 200 °C between $\epsilon = 0.6$ and 0.8. Besides the influence of carbonisation degree, they also found a decreasing trend of the emissivity with higher temperatures. Via emission/transmission spectroscopy at 300–782K, Solomon et al. [7,8] confirmed the influence of the fuel's degree of carbonisation and found an influence of the fuel degree of pyrolysis, resulting in the observation of a non-grey, and therefore wavelength dependent emission behaviour. These results were further confirmed and extended by Bhattacharya and Wall [9], where the investigations of thin layers of coal chars at temperatures up to 1000 °C showed a dependence of the emissivity from the coal type, temperature, particle diameter and conversion progress. Furthermore, in the wavelength range from 2 to 5 µm the non-grey behaviour was confirmed with emissivity variations between $\epsilon = 0.6$ and 0.85. Single particle emissivities in combustion systems were first measured by Rego-Barcena et al. [10]. At a wavelength range of 3.95 µm the particle emissivity was proven to be temperature dependent. Furthermore, Bäckström et al. [11] measured the emissivities at different flame locations, varying from $\epsilon = 0.15$ to 0.45. Overviewing all these studies and their individual findings, Yin [12] concluded that the available literature data of fuel emissivities were still incomplete, even though they are highly mandatory for simulations.

18.2.2 Emissivity Definition

The wavelength-dependent total emissivity of a single fuel particle describes its ability to emit radiation at a specific wavelength λ. The total radiation intensity of the particle emitted at this wavelength I_{P_λ} is compared to the respective intensity I_{BB_λ} emitted by a theoretically identical blackbody radiator, given by:

$$\epsilon_{P_\lambda} = \frac{I_{P_\lambda}}{I_{BB_\lambda}} \tag{18.1}$$

The emitted radiation intensity of the blackbody depends on the particle surface area A and temperature T, as given by the Stefan-Boltzmann law for a blackbody radiator:

$$I_{\mathrm{BB}} = \sigma \, A \, T^4 \tag{18.2}$$

As shown in Chaps. 2 and 3, the composition of an individual fuel particle changes during burnout, raising the question how composition and structural changes affect the particle emissivity as the particle reacts. Consequently, the total emitted radiation as well as the individual temperature and surface area of single reacting particles during their burnout need to be determined experimentally. In the following, the received particle parameters are compared to reference radiation intensities received via calibration measurements of a blackbody reference radiator.

18.2.3 Experimental Setups

For the experimental determination of the particle size, temperature, and total emitted radiation intensity during burnout, two different setups were applied. While the first setup by Graeser and Schiemann [13] is used for investigations of particles in a laminar flow reactor (LFR), the second setup by Pörtner et al. [14] observes laser-induced burnout of single particles in a single particle reactor (SPR). The laminar flow reactor setup is used to determine particle parameters at different, but limited, particle reaction times, while the single particle setup provides results for the entire reaction time of a single particle. Both setups are schematically illustrated in Fig. 18.1.

In the LFR setup of Graeser and Schiemann [13], the radiation emitted by the burning particles in the laminar flow reactor is captured by a 90° off-axis parabolic mirror and focused onto a coded aperture. This aperture is used to measure the particle size, as it has several slits of defined size that allow to determine the average diameter of the particle from the shape of the detector signals. The radiation passing this aperture is collimated by a second 90° off-axis parabolic mirror and guided to a polka-dot filter. As this filter has an array of reflecting and transmitting areas, the particle radiation is splitted into two identical parts. The reflected part of the radiation is focused by a CaF_2 lens onto an IR detector, which records the total emitted radiation intensity. Either an InSb detector with an operation wavelength range in the mid infrared region (MIR) from 2.4–5.5 μm or a spectrometer with an operation wavelength range in the near infrared region (NIR) from 1.25–2.25 μm is applied. Radiation that is not reflected by the polka-dot filter passes through it and hits a beam splitter cube, which splits the incident radiation into three different parts by multiple surface reflections. Two of the resulting beams are spectrally filtered, using narrow bandpass filters with central wavelengths of 550 ± 10 nm and 700 ± 10 nm. Each of the beams is focused onto a photomultiplier tube (PMT), which records the intensity of the incident particle radiation in the respective spectral range. The intensities measured by the PMT are then used to determine the particle temperature through two-colour pyrometry.

When measuring the total emitted radiation, it is essential to ensure that a measured particle is located in the centre of the probe volume. Therefore, a He-Ne laser is

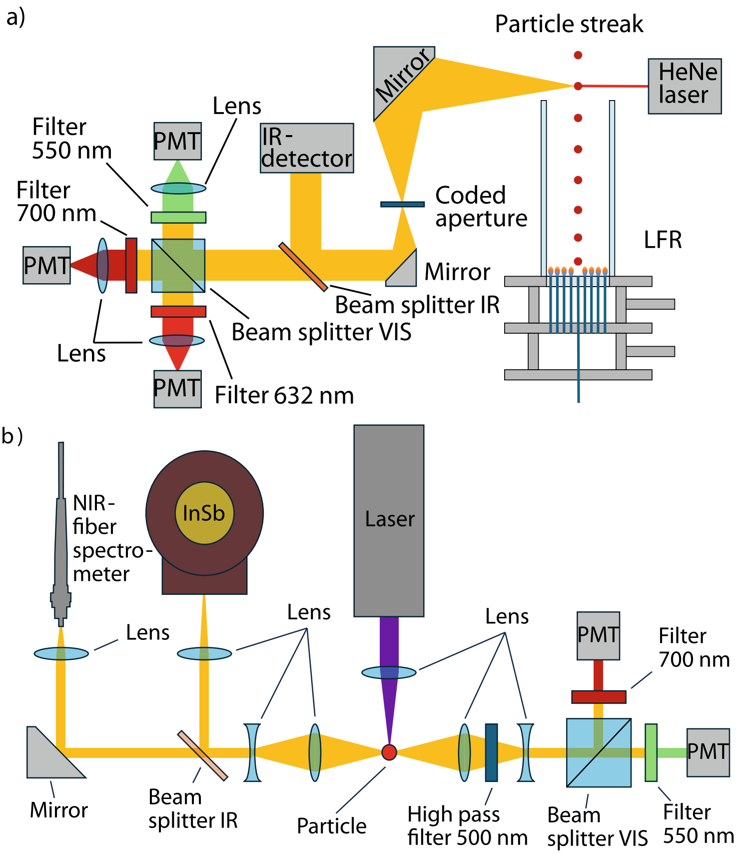

Fig. 18.1 Experimental setups for the determination of fuel particle emissivity **a)** in a laminar flow reactor (reprinted from Graeser and Schiemann [13], Copyright (2016), with permission from Elsevier) and **b)** for the determination of fuel particle emissivity via laser-induced single particle burnout [14]

focused on the centre of the beam using a 90° off-axis parabolic mirror. The laser radiation scattered by the particle is also captured by the previously described setup and directed to a third PMT. This PMT is equipped with a narrow band filter with a central wavelength of 632 ± 10 nm, which ensures the detection of laser radiation only.

A laser-induced ignition setup is used for single fuel particle investigations in the SPR. A single particle is positioned on a mechanical support at the centre of the setup and ignited by a diode laser. The diode laser emits radiation with a total power of 1.2 W at 450 nm, which is focused onto the particle via a biconvex lens. After the particle is ignited, the radiation emitted by the particle is analysed in different spectral ranges.

Similar to the optical setup on the LFR, the emitted particle radiation is collected by a lens system and directed onto a 50:50 beam splitter for particle temperature determination by two-colour pyrometry. A high-pass filter with a cutoff wavelength of 500 nm suppresses scattered laser radiation from the particle surface. Prior to detection by two PMT, the particle radiation is spectrally filtered using narrow bandpass filters with central wavelengths of 550 ± 10 nm and 700 ± 10 nm.

In contrast to the LFR setup, the two infrared detectors of the SPR setup are used simultaneously to determine the total emitted radiation intensity of the particle. The emitted particle radiation is collected by a CaF_2 lens system and directed to an infrared 50:50 beam splitter for simultaneous detection in the NIR (1.25–2.25 μm) and MIR (2.4–5.5 μm) spectral ranges.

18.2.4 Methods

The determination of the individual particle parameters during burnout is based on reference calibration measurements performed on a blackbody reference radiator. The respective reference data sets contain temperature, diameter, and total emitted radiation calibrations, which are outlined in the following.

As discussed, in the laminar flow reactor (LFR) setup of Graeser and Schiemann [13], the determination of the individual particle diameter is performed by the coded aperture. As a particle moves through the probe volume, two signal intensities I_1 and I_2 are recorded using the specific aperture shown in Fig. 18.2. It can be shown, that this aperture leads to an intensity ratio I_1/I_2 which is proportional to the particle diameter D_P.

$$I_\mathrm{r} = \frac{I_1}{I_2} \sim D_\mathrm{P} \tag{18.3}$$

To determine the diameter for various intensity ratios, the system was calibrated simulating radiating moving particles of different sizes. Radiating moving particles were simulated by a backlit rotating disc with various precision pinhole apertures. The different pinhole diameters cause varying intensity ratios detected with the PMT. An illustration of the coded aperture with a single particle (yellow dot) and the resulting ratios of the reference signal peaks, together with a linear regression function, are shown in Fig. 18.2.

In contrast to this procedure, in the single particle experiments of Pörtner et al. [14] in the SPR, the particle diameter was assumed to be constant. Therefore, the results presented later must be treated with caution, as the variation in particle diameter has a large effect on the emissivity determined.

Two-colour pyrometry is used to determine the particle temperature in both setups, the LFR and SPR, using the radiation intensities I_{550} and I_{700} at 550 ± 10 nm and 700 ± 10 nm, and calculating their ratio I_r

$$I_\mathrm{r} = \frac{I_{550}}{I_{700}}. \tag{18.4}$$

To assign an intensity ratio obtained from the particle experiments to the respective temperature, calibration measurements using a blackbody reference were performed

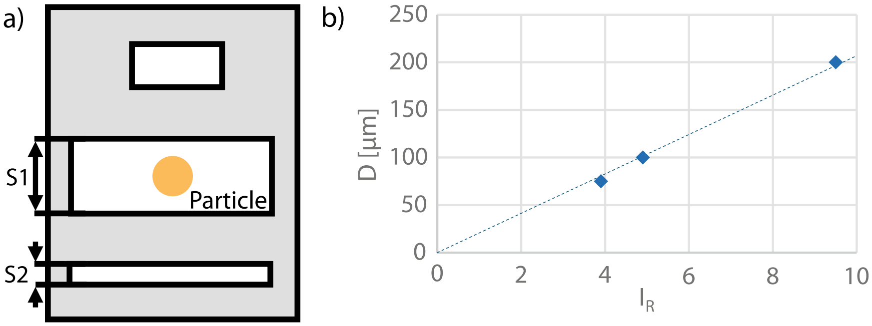

Fig. 18.2 **a)** Schematic illustration of the coded aperture with the defined slit sizes S1 and S2. (reprinted from Graeser and Schiemann [13], Copyright (2016), with permission from Elsevier) and **b)** diameter *D* calibration curve determined by precision pinhole experiments [15]

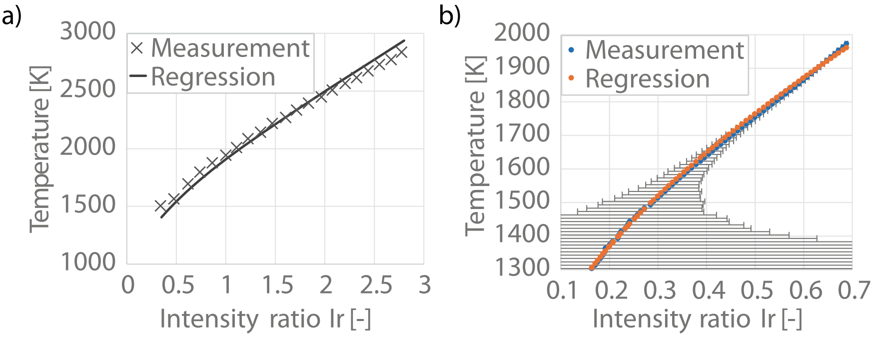

Fig. 18.3 **a)** Temperature calibration curve of the laminar flow reactor setup [16] and **b)** temperature calibration curve of the single particle setup [14]

for both experiments. For varying radiator temperatures, the radiation intensities I_{550} and I_{700} of the reference radiation were recorded by the PMT, resulting in temperature dependent intensity ratios I_r. Via the definition of I_r and Wien's radiation law, the relation between the measured intensity ratio and the temperature of the observed blackbody radiator is given in the study by Graeser et al. [16] as

$$T = \frac{h\,c_0\,(\lambda_1 - \lambda_2)}{k_\mathrm{B}\,\lambda_1\,\lambda_2}\left[\ln\left(\frac{1}{\kappa}\left(\frac{\lambda_1}{\lambda_2}\right)^5\right) + \ln\left(I_\mathrm{r}\right)\right]^{-1} \tag{18.5}$$

A regression of (18.5) on the measured intensity ratios via the fit coefficient κ leads to the calibration curves of both setups shown in Fig. 18.3. This allows to determine the particle temperature for a wide range of particle radiation intensity ratios. Note that the fit coefficient κ is different for the two optical setups, as it takes into account all individual setup radiation intensity losses. Caused by the measurement uncertainties, this method is only valid for temperatures above 1550 K.

For each possible particle temperature and size, a respective blackbody radiation intensity is mandatory to determine the particle emissivity. For the determination

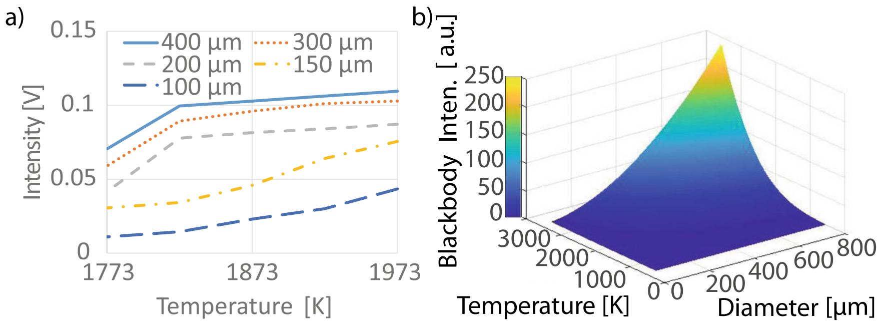

Fig. 18.4 **a)** Measured blackbody reference data for the laminar flow reactor setup. The different lines denote different diameters of the pinholes as specified in the legend (reprinted from Graeser and Schiemann [13], Copyright (2016), with permission from Elsevier). **b)** Reference surface determined from the calibration measurements of the single particle setup [14]

of this reference radiator intensity I_{BB}, the optical setup needs another calibration. The respective optical part of each setup is positioned in front of a blackbody reference radiator, which was equipped with precision pinhole apertures of varying size. These apertures were positioned between the optical setup and the blackbody reference radiator in the probe volume of each individual setup. The signal intensities received from the NIR-spectrometer and the InSb detector (MIR) were recorded for all pinhole diameters and varying temperatures and thus, form the intensity reference data. These data sets were interpolated to provide reference intensities also for particle temperature and diameter combinations not represented by the chosen reference radiator temperatures and pinhole diameters. Illustrations of the reference data sets in the MIR are presented for both setups in Fig. 18.4.

18.2.5 Results

Colombian Coal Particle Emissivity with Carbon Conversion Evolution

The carbon conversion evolution of the single particle emissivity of Colombian coal bituminous (CBC) particles was investigated by Graeser et al. [17, 18]. The particle emissivity was measured in the laminar flow reactor at five different heights of the burning particle streak, covering early and late char burnout regions. Conversion identification was performed by taking particle samples from the streak at the corresponding emissivity measurement heights, applying a water-cooled, nitrogen-purged sampling probe. The ultimate analysis results are shown in Table 18.1 while the measurement heights as well as the determined emissivity and conversion is displayed in Fig. 18.5. With increasing ash content, the carbon conversion continuously rises from 49% at a height of 12.5 cm to 62% at a height of 22.5 cm. At the same time, as the conversion of the particles increases, the emissivity in both spectral regions decreases. In the NIR, the emissivity decreases almost linearly from 0.53 at a height

Table 18.1 Results of the ultimate analysis (dry basis), ash yield a_{Sample} (dry basis), and carbon related conversion *c* at different heights of the flat flame burner combustion chamber from Graeser and Schiemann [17]

Height [cm]	C (± 1.6) [wt.%]	H (± 0.1) [wt.%]	N (± 0.1) [wt.%]	a_{Sample} (± 0.3) [wt.%]	c [%]
0.0	72.4	4.6	2.0	5.9	0
12.5	82.3	1.0	2.2	12.4	49±3.3
15.0	85.1	0.4	1.8	13.1	50±3.2
17.5	83.7	0.2	1.5	13.9	54±2.9
20.0	82.2	0.2	1.4	14.7	57±2.7
22.5	81.1	0.3	1.3	16.3	62±2.4

Table 18.2 Results of the ultimate analysis (dry basis), ash yield a_{dry} (dry basis) and carbon related conversion *c* of the initial fuel samples and samples taken from the particle streak of the LFR [19]

	Initial fuel sample		Taken from LFR	
	SiO_2-HTC [%]	Fe_2O_3-HTC [%]	SiO_2-HTC [%]	Fe_2O_3-HTC [%]
C	66.4	67.7	70.4±1.6	69.6±1.6
H	3.9	4.5	3.6±0.1	3.6±0.1
N	0.3	0.8	0.6±0.1	0.8±0.1
O	29.4	27.0	25.5±1.8	26.0±1.8
a_{dry}	3.2	23.2	5.4±0.3	33.7±0.3
c	0.0	0.0	39.0±13.0	40.0±3.0

of 12.5 cm to 0.41 at 22.5 cm. Confirming this trend, the emissivity data in the MIR decreases from 0.70 at 12.5 cm to 0.63 at 22.5 cm.

Influence of Fuel Mineral Content on the Emissivity of Synthetic Carbonaceous Fuel

To investigate the influence of the fuel mineral content on the total particle emissivity, Graeser et al. [19] performed emissivity measurements in the LFR on two samples of a synthetic carbonaceous fuel (HTC). Further details on HTC generation can be found in the study by Graeser et al. [19] and Sect. 4.2. As SiO_2 and Fe_2O_3 are important coal ash constituents, both samples were doped with 5% SiO_2 and one of the samples with additional 25% Fe_2O_3. The sample's emissivities were investigated in the previously described setup at a height of 7.5 cm above the burner surface in an oxy-fuel atmosphere containing 25% O_2, 56% CO_2, and 19% H_2O. Fuel samples were taken at this burner height to provide information on particle conversion. The ultimate analysis results of the two initial HTC samples and fuel samples taken at a burner height of 7.5 cm are presented in Table 18.2.

A composition comparison of the raw fuel and the samples taken at a burner height of 7.5 cm show an increasing carbon and decreasing hydrogen content with burnout. Additionally, the ash yields increase and the resulting conversions are comparable for both samples. The results of the emissivity measurements are presented in Fig. 18.6.

In both spectral ranges (NIR and MIR), the Fe_2O_3-doped sample exhibits significantly higher mean and median emissivity compared to the sample doped solely with SiO_2. With a difference of 0.13 in the NIR, this effect is slightly more pronounced in this spectral range compared to the MIR, where the difference is 0.10. Possible explanations include the additional doping process with iron oxide, which could induce changes in particle structure and/or porosity, that are known influencing factors [20]. Additionally, catalytic effects of Fe_2O_3 and heterogeneous mineral distributions within the fuel may have influenced the fuel structure. Furthermore, determined single particle emissivities with values above 1 are caused by measurement method uncertainties.

Temperature Dependence of Colombian Bituminous Coal Particle Emissivity The influence of the particle temperature on single bituminous Colombian coal particles (CBC) was investigated in the LFR by Graeser and Schiemann [21]. An analysis of the raw coal sample with a sieve fraction of 160–200 µm showed a carbon content of 72.4%, hydrogen content of 4.6%, and nitrogen content of 2.0%. The ash yield of the samples was determined to be 5.9%. For the measurements in the laminar flow reactor, the oxygen concentration of the reaction atmosphere was varied to achieve different particle temperatures. Since the char oxidation rate is directly linked to the oxygen partial pressure, this adjustment increased the reaction temperature and consequently the particle temperature. To cover a broad spectrum of particle temperatures, the oxygen content ranged from 15 to 40%. Table 18.3 presents a list of all examined reaction atmospheres, their respective average temperatures, and the subsequently determined average particle temperatures from two-colour pyrometry measurements.

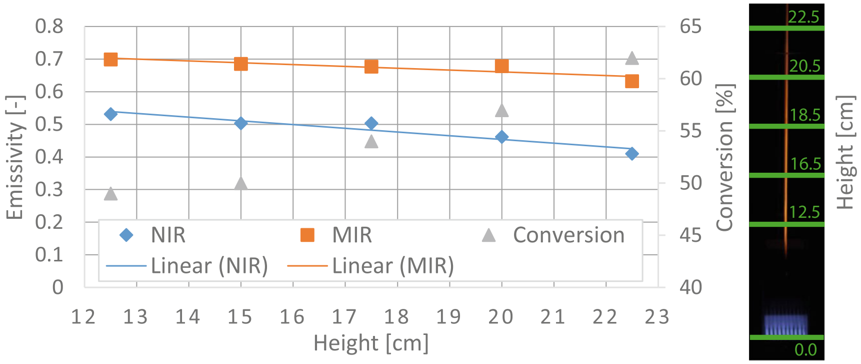

Fig. 18.5 Average total emissivity (left ordinate) in the spectral range from 1.25–2.25 µm and 2.4–5.5 µm, and the carbon conversion (right ordinate) at each level (left) (reprinted from Graeser and Schiemann [18], Copyright (2018), with permission from Elsevier) and image of a particle streak including lines for measurement level height illustration (right)

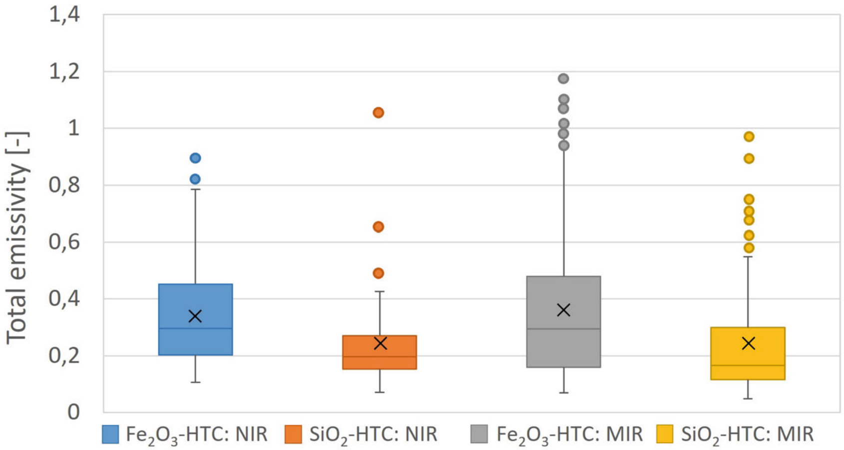

Fig. 18.6 Boxplot of the average total emissivity in two spectral ranges from 1.25–2.25 µm and 2.4–5.5 µm of both char samples at a burner height of 7.5 cm [19]

Table 18.3 Composition of the reaction atmospheres and their influence on the particle temperature for the investigation of the emissivity from Graeser and Schiemann [21]

Nr.	Atmosphere composition			Gas temperature [K]	Particle temperature [K]
	O_2 [vol.%]	CO_2 [vol.%]	H_2O [vol.%]		
1	15.0	66.0	19.0	1767	1956
2	17.0	64.0	19.0	1776	2028
3	19.0	62.0	19.0	1788	2071
4	21.0	60.0	19.0	1796	2109
5	23.0	58.0	19.0	1808	2149
6	25.0	56.0	19.0	1819	2189
7	30.0	51.0	19.0	1844	2378
8	35.0	46.0	19.0	1873	2458
9	40.0	41.0	19.0	1902	2548

The measurements were conducted at a fixed elevation of 15 cm above the burner surface. At this level, devolatilisation had already completed and pure char burnout was observed. Emissivity was measured in both the NIR and MIR spectral regions. The averaged emissivity of both spectral ranges, dependent on the corresponding average particle temperature of each atmosphere, is illustrated in Fig. 18.7.

In both spectral ranges, the predominant trend is a decrease in emissivity with increasing particle temperature. In the NIR, emissivity steadily declined from 0.33 at 1972 K to 0.23 at 2180 K. For higher temperatures, values remained relatively constant at around 0.21. In the MIR, emissivity decreased linearly across the entire temperature range, from 0.54 at 1950 K to 0.26 at 2545 K.

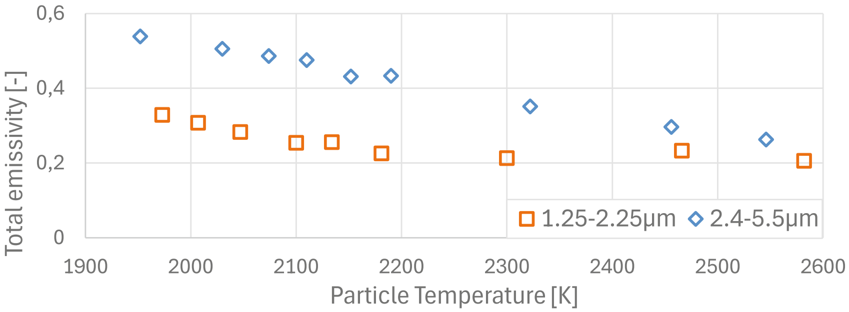

Fig. 18.7 Spectrally averaged emissivity in dependence on the particle temperature for both wavelength ranges (reprinted from Graeser and Schiemann [21], Copyright (2020), with permission from Elsevier)

Time-Resolved Single Coal and Biomass Particle Emissivity

Time resolved single fuel particle emissivity analysis were performed by Pörtner et al. [14] in the SPR setup. Within this study, Colombian bituminous coal (CBC) and walnut shell (WNS) particles were investigated. Based on the raw sample size fraction limits, the coal particles were assumed to have an average diameter of 180 µm and the walnut shell particles an average diameter of 325 µm. Ultimate and proximate analysis of the two fuels is reported in Table 1.1.

Pörtner et al. [14] investigated five different coal and six walnut shell particles. The results of each particle were restricted to a reliable region, excluding low signal intensities and the devolatilisation process. The resulting pairs of particle temperature and respective emissivity were sorted into temperature groups of 100 K width. The resulting temperature dependent distribution of the fuel particle emissivities is presented in Fig. 18.8.

For both fuels, the dominant trend is a decrease in emissivity with increasing particle temperature, in agreement with results from the study by Graeser and Schiemann [21] using the same coal. The overall emissivity of walnut shells decreases from 0.17 at 2100 K to 0.04 at 2900 K. In comparison, the emissivity of coal is consistently higher, decreasing from 0.4 at 2300 K to 0.01 at 3400 K. This difference between coal and walnut shell particles can be assigned to the significantly higher volatile content of the walnut shells compared to the coal, as therefore, the char burnout of the walnut shells is inhibited. Consequently, the char burnout of the coal particles starts earlier, which leads to slightly higher burnout temperatures.

18.3 Normal Spectral Radiative Emittance of Ash Layers Under Oxy-Fuel Conditions

Ashes from solid fuel combustion form deposits on heat exchanger surfaces in boilers. These deposits influence the heat transfer from the flame to the heating surfaces. This is particularly critical in the furnace section, where radiation dominates and the

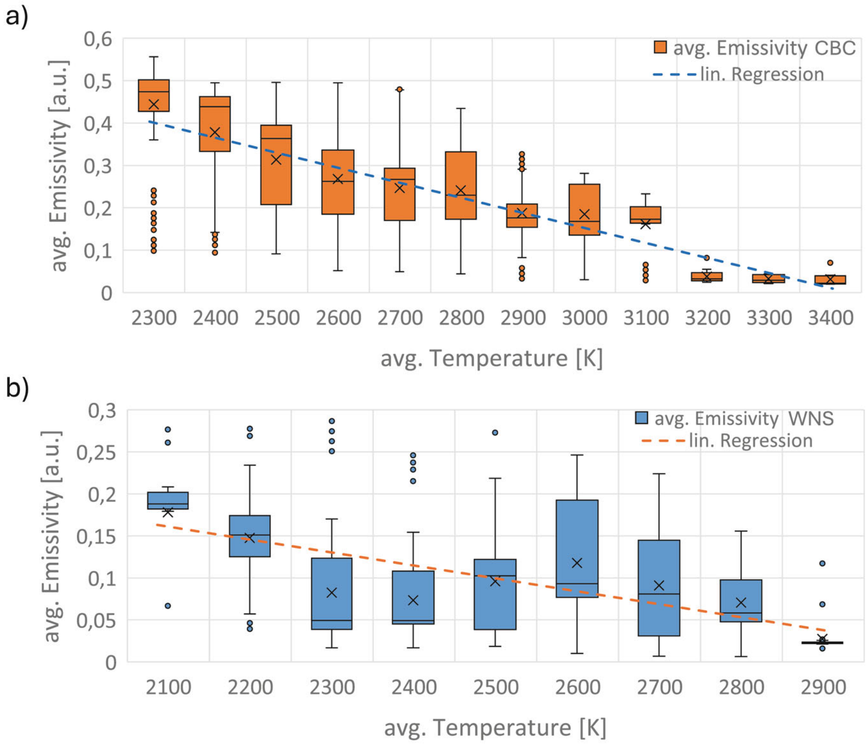

Fig. 18.8 Temperature-dependent emissivity of **a)** Colombian bituminous coal (CBC) and **b)** walnut shell (WNS) particles [14]

emittance properties of the ash layer play a key role. Consequently, spectral dependence of radiative emittance is important for boiler layout. Coal ashes are strongly non-grey, which has to be considered in spectrally resolved CFD simulations, or if non-spectrally resolved radiation balances are carried out, appropriate averaging of the spectral emittance has to be accounted for (e.g. a weighted averaging procedure with Planck's law as weighting function [22]). Please note, even if this section concentrates on coal ashes, it is expected that the general results can be transferred to other fuels as biomass.

Already in 1969, Boow and Goard [2] concluded that the emittance is influenced by the structure of the surface (mean particle size, roughness of the layer) and by the mineral composition of the ashes. In the studies by Shimogori et al. [23] and Saljnikov et al. [24], it is shown that spatially averaged total emittance is decreasing with increasing ash temperature. Correlations of emittance as a function of particle diameter are reported for synthetic ash layers by Boow and Goard [2] and Greffrath et al. [20] with decreasing emittance for smaller particle diameter. This dependency was confirmed, e.g. by Wall et al. [25], based on Mie theory and for real coal ashes by measurements of Markham et al. [26]. Surface sintering at elevated temperature increases emittance as well as surface fusion as reported by Boow and Goard [2].

Greffrath et al. [5] showed that fusion—depending on the ash composition—can either increase emittance (formation of glass-like layers) or can decrease emittance (formation of a mirror-like surface). The Fe_2O_3 acts as a so-called colouring agent that increases emittance of ash layers. Shimogori et al. [2] and Shimogori et al. [27] presented a correlation of the spectral emittance of coal ashes as a function of Fe_2O_3 content. Boow and Goard [28] verified the influence of Fe_2O_3 and the measured complex refractive index of slags as a function of composition. All these studies mentioned-above are not related to the specifics of oxy-fuel combustion. Oxy-fuel firing systems—compared to air fired systems—have significantly higher CO_2 concentrations in the combustion zone but also show an increased concentration of minor species like SO_2 due to intensive flue gas recirculation. Consequently, oxy-fuel ashes might contain more carbonates and sulphates than ashes from air-fired systems. However, the statements in literature whether carbonates or sulphates dominate in oxy-fuel ashes are contradictory.

Against this background, the spectral characteristics of the emittance for typical carbonates and sulphates found in coal ashes were investigated. Due to space limitations, this chapter will focus on $CaCO_3$ and $CaSO_4$, as calcium is commonly present in significant quantities in coal ash and can form both carbonates and sulphates. For comparison, K_2SO_4 is also included in the analysis. Note that further detailed studies on the emittance of Ca-, Mg-, and Sr-carbonates as pure substances and mixed with SiO_2 have been conducted [22,29]. The minerals $CaCO_3$, $CaSO_4$, and K_2SO_4 were prepared in powder form and sieved into two particle size fractions. Results are presented for $CaCO_3$ and $CaSO_4$ with a particle size fraction of $x = 125–160\,\mu m$, and for K_2SO_4, results are also shown for the finer fraction of $x < 32\,\mu m$.

18.3.1 Experimental Setup

The measurements of thermal radiation were carried out in a facility, where samples are heated to temperatures ranging from 500 to 1000 °C. The test rig consists of a Fourier-transform infrared (FTIR) spectrometer and an electrical heating unit. The heating unit contains both, a sample holder and a blackbody as reference radiator. The radiation emitted by the heated sample (22 mm diameter, 2 mm thickness) and the blackbody is directed to the FTIR spectrometer using a gold-coated off-axis parabolic mirror. Thermal radiation is detected in the range from 1.6–12 μm. The sample surface temperature is determined by two thermocouples (type K, 0.25 mm diameter) installed 1 and 2 mm below the sample surface (in the central axis of the disc-shaped sample). A schematic illustration of the setup is presented in Fig. 18.9.

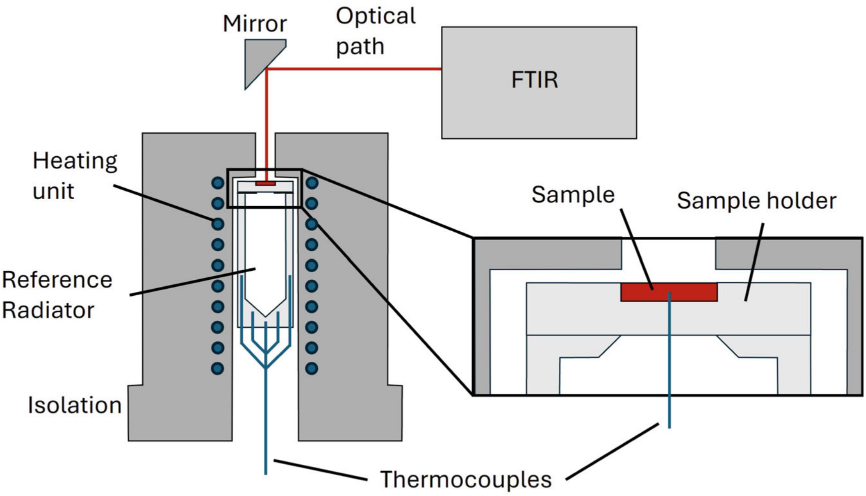

Fig. 18.9 Experimental setup for material emissivity determination

18.3.2 Methods

In order to obtain the spectral normal emittance in (18.6), the sample radiation $S_{\mathrm{sample}}(\lambda, T)$ is compared with the radiation of the blackbody $S_{\mathrm{BB}}(\lambda, T)$:

$$\epsilon(\lambda, T) = \frac{S_{\mathrm{sample}}(\lambda, T)}{S_{\mathrm{BB}}(\lambda, T)} \tag{18.6}$$

The total average emissivity in a spectral range between λ_1 and λ_2 results from:

$$\overline{\epsilon}(T) = \frac{\int_{\lambda_1}^{\lambda_2} S_{\mathrm{sample}}}{\int_{\lambda_1}^{\lambda_2} S_{\mathrm{BB}}} \tag{18.7}$$

The sample surface temperature is calculated by assuming a linear temperature profile across the sample's thickness. Consequently, the probe surface temperature is determined via the measured temperatures of the thermocouples located at the bottom and the centre of the sample.

18.3.3 Results

As examples for carbonates and sulphates, the spectral emittances of $CaCO_3$, $CaSO_4$, and K_2SO_4 are shown in Fig. 18.10.

The general trend of the spectral emittance is similar and typical for minerals, i.e. also for coal ashes. The spectral emittance is small at low temperatures and increases with wavelength to values in the order of 0.8–0.9 above 10 µm. The spectral

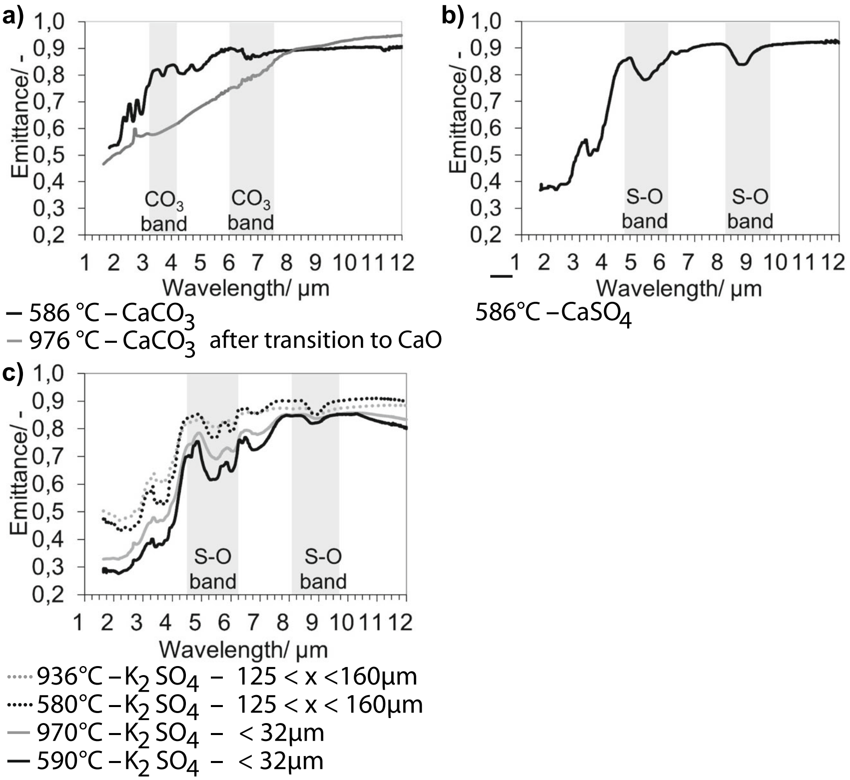

Fig. 18.10 Spectral emittance of **a)** $CaCO_3$, particle size fraction $x = 125–160\,\mu m$, **b)** $CaSO_4$, particle size fraction $x = 125–160\,\mu m$, and **c)** K_2SO_4, particle size fractions $x < 32\,\mu m$ and $x = 125–160\,\mu m$

emittance of the carbonates and sulphates show characteristic spectral bands due to the presence of the CO_3 and the S–O functional groups. Note that the specific bands around 3 µm in Fig. 18.10 are to the presence of CO_2 in the surrounding air.

Figure 18.10a) presents the spectral emittance for $CaCO_3$ for the particle size fraction $x = 125–160\,\mu m$. Spectral bands of the characteristic CO_3 group are shaded in grey. Thermodynamic calculation carried out with *FactSage* predict a decomposition at 775 °C for $CaCO_3$ to CaO. Thus, $CaCO_3$ is completely decomposed at 976 °C as confirmed by X-ray diffraction measurements. The phase transition from $CaCO_3$ to CaO is clearly visible in Fig.18.10a), with a noticeable reduction in emittance during the transformation and the characteristic spectral peaks of $CaCO_3$ disappear.

Comparing Figs. 18.10a) and b), it is evident that the spectral emittance of calcium carbonate (Fig. 18.10a)) is higher than that of the corresponding sulphates (Fig. 18.10b)) up to a wavelength of approximately 4.5 µm. Above 4.5 µm, the spectral emittance of $CaCO_3$ and $CaSO_4$ are similar in the order of 0.9. Also $CaSO_4$ (Fig. 18.10b)) exhibits characteristic bands but they occur at different wavelength ranges compared to $CaCO_3$. Note that $CaSO_4$ remains stable at the typical temperatures of coals ashes in boilers, indicating that the S–O bands can also been detected in real coals ashes, which have been exposed to very high temperatures.

Figure 18.10c) shows the characteristic S–O bands as well for K_2SO_4. Instead, K_2SO_4 shows no phase transformation even at elevated temperature similar to $CaSO_4$. Figure 18.10c) clearly shows that larger particle sizes result in higher emittance, a well-documented effect for coal ashes in general [23].

This section about spectral emittance of coal ashes with respect to oxy-fuel conditions cannot cover all aspects. For example, values for total emittance as a function of temperature for carbonates and sulphates can be found in the study by Gorewoda and Scherer [22]. Detailed studies on the influences of particle size on emittance are presented by Gorewoda et al. [30] and Gorewoda [31]. Furthermore, it has been shown that the characteristic emittance bands of carbonates and sulphates can be found in real coal ashes [31].

18.4 Scattering Experiment

The complex index of refraction IOR is a mandatory material property to determine the radiative characteristics of solid fuel particles. In this section, two experimental setups are presented for the measurement of the IOR. These experiments aim to measure the scattered intensity in multiple spatial directions and then analyse the scattering pattern to determine the IOR. A crucial condition is to apply non-intrusive methods to avoid falsification of the radiation interaction with the particle. Both setups achieve this goal differently. The first setup utilises an acoustic levitator (setup A). The second setup achieves this condition using a flat flame burner (setup B). In the following section, these two setups are described and measurement results are presented.

18.4.1 Setup A: Acoustic Levtiator

Figure 18.11 displays setup A. As the complex index of refraction is wavelength-dependent, a broadband source is required. Therefore, a silicon carbide light source was used as a source for scattering radiation from particles, with radiation in the range of 0.5–9 μm. The temperature of the silicon carbide light source is kept constant to ensure constant emission intensity. An ellipsoid reflector and a CaF_2 lens are used to focus the emitted radiation on the particle.

The particle is kept contactless in position by the acoustic levitator. The levitator consists of 2 shells, each with four speaker rings equipped with 4, 8, 16, and 16 sound sources. Each sound source points towards the centre of the levitator. The emitted sound waves superimpose in the levitator, creating an interference pattern and resulting in a standing sound wave. The sound pressure creates a force on the particle, which compensates the gravitational force. Further details and explanations of the basic principle are explained by Marzo et al. [32].

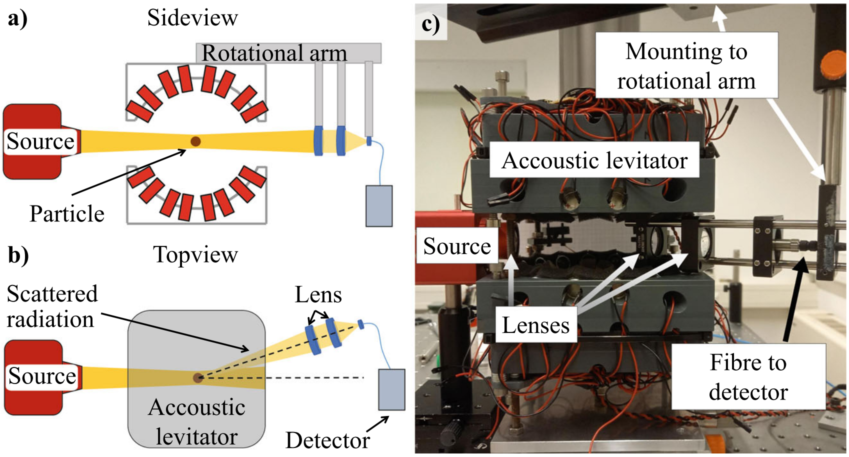

Fig. 18.11 Experimental setup A: Radiation is focused on a levitating particle and the scattered radiation is collected by lenses: schematic illustration of the setup in **a)** sideview and **b)** topview, as well as **c)** a picture of the setup

The radiation interacts with the levitated particle and is finally scattered in different spatial directions. This scattered radiation is collected by lens optics, which are mounted to an angle adjustable arm. The centre of the rotational axis coincides with the z-axis and thus with the position of the particle. The lens optics consists of two CaF_2 lenses, both with a lens diameter $D_L = 25.4$ mm and a focal length $f_L = 40$ mm. The first lens collects the scattered radiation and collimates it. The second lens focuses the collimated radiation onto the end of an indium fluoride glass fibre.

During the experiments, scattering angles $\theta = 21$–$114°$ were investigated. For $\theta \geq 114°$, the radiation collecting lenses block the path between particle and source. For $\theta \leq 21°$ the fraction of emitted radiation that radiates directly from the source into the lens optics falsified the measurement.

For the evaluation of scattered radiation, either an FTIR spectrometer from *ARCoptix* was used (supporting wavelengths ranging from $\lambda = 2000$ to 6000 nm) or a spectrometer for the visible and near infrared range from *Oceanview* (supporting wavelengths ranging from $\lambda = 200$ to 1100 nm).

18.4.2 Setup B: Flat Flame Burner

The distribution of radiation scattered by single particles of a particle streak was measured by the setup illustrated in Fig. 18.12.

The particle streak in this setup is either provided by a flat flame burner (burning particles) or a feeding system doping cold particles through the centre of the setup. To provide radiation of a wide wavelength range, a 1 kW Xe-band lamp is focused via two parabolic 90° off-axis mirrors onto the streak. While transmitted lamp radiation is reflected by another mirror into a beam trap, the scattered radiation

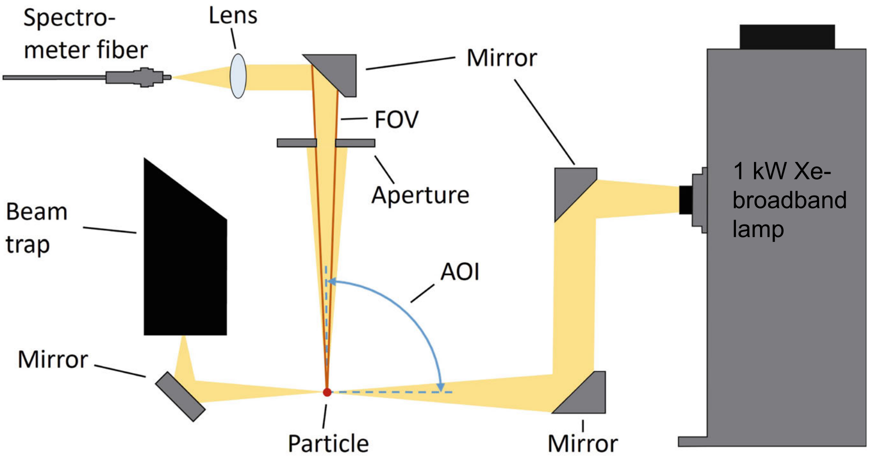

Fig. 18.12 Schematic illustration of the experimental setup B for investigations of the radiation scattering phase function of a particle streak

distribution is measured by a detection unit. The radiation redirected by the particle passes an aperture of 25.4 mm, which defines the field of view (FOV). The radiation is collimated by a 90° off-axis parabolic mirror and focused by a CaF_2 lens into the fibre of a spectrometer sensitive to a wavelength range of 200–1000 nm. For the determination of the radiation distribution, the angle of incidence (AOI) of the lamp radiation is varied via a rotation stage.

18.4.3 Assessment of the Phase Function

In both experimental setups, a circular optic is used to collect the scattered radiation. To evaluate the phase function, it is integrated over the circular area of the collection optics

$$\Phi_{\Delta\theta,i} = 2 \int\limits_{\theta^* - \frac{\Delta\theta}{2}}^{\theta^* + \frac{\Delta\theta}{2}} \Phi \sin(\theta) \sin(\varphi^*)\, d\theta, \tag{18.8}$$

where θ^* is the angular position of the collecting optic. The integration width $\Delta\theta$ is related to the optics diameter D_L and its focal length f_L:

$$\Delta\theta = \arctan\left(\frac{D_L}{f_L}\right) \tag{18.9}$$

The factor $\sin(\varphi^*)$ considers the integration over a circular element. These angles and parameters are illustrated in Fig. 18.13.

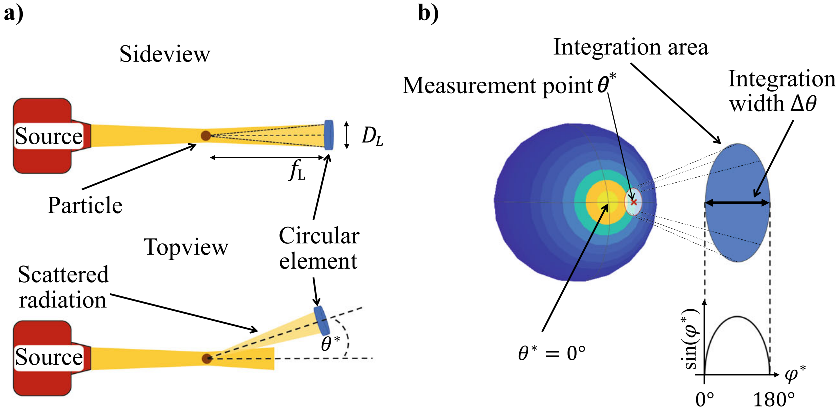

Fig. 18.13 **a)** Side- and topview of the scattered radiation, which is collected by a circular element and **b)** phase function plotted on a particle and the relation of θ^* and $\sin(\varphi^*)$ in (18.8)

18.4.4 Resulting Complex Index of Refraction

To determine the complex index of refraction, an inverse problem is solved, which is transferred into an minimisation problem

$$\min\left[\Delta\Phi(\mathrm{IOR})\right] \tag{18.10}$$

with the functional $\Delta\Phi(\mathrm{IOR})$,

$$\Delta\Phi = \sum_{i=1}^{N_{\theta*}} \frac{\mathrm{abs}\left(\log(\Phi_{\Delta\theta_i,\mathrm{Calc}}) - \log(\Phi_{\Delta\theta_i,\mathrm{Meas}})\right)}{\mathrm{abs}\left(\log(\Phi_{\Delta\theta_i,\mathrm{Calc}})\right)} \tag{18.11}$$

The indices “Meas” and “Calc” are short for measured and calculated. This function resembles the relative difference between measured and calculated integrated phase function. This difference is minimised by changing the complex index of refraction IOR.

Figure 18.14 exemplary illustrates the fit of the measured index of refraction for walnut shells (WNS) utilising setup A (Fig. 18.14a)) and the wavelength-dependent IOR of cold and burning Colombian bituminous coal (CBC) particles from setup B (Fig. 18.14b)).

Comparing the real and imaginary parts of reacting and non-reacting coal particles, the received values show an approximately constant behaviour in the visible spectral range. In contrast to this, the walnut shells showed a clear increase of both IOR parts with wavelength. Please note, the received IOR parts of the walnut shells were determined for a spectral range of 2–5.5 μm, differing from the coal results.

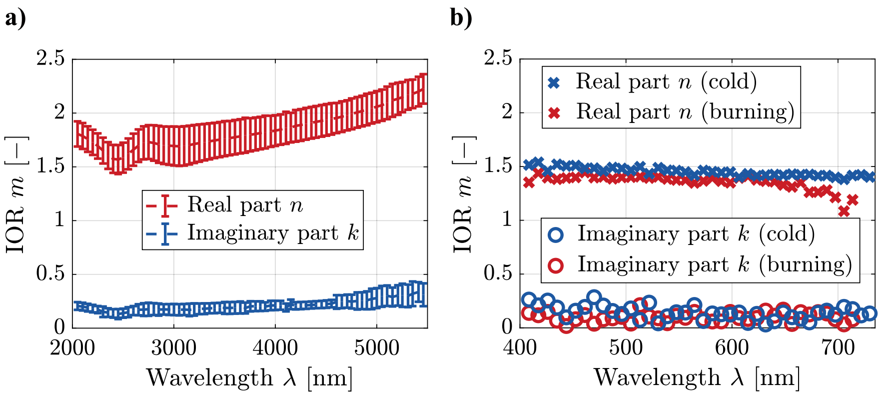

Fig. 18.14 Wavelength dependent complex index of refraction (IOR) of **a)** walnut shell particles determined by setup A (reprinted and slightly adapted from Koch et al. [33], licensed under CC BY 4.0) and **b)** reacting and non-reacting coal particles determined by setup B (reprinted from Koch et al. [34], Copyright (2021), with permission from . and minor editing)

18.5 Conclusion

This chapter has presented several different approaches to the experimental investigation of the radiative effects that contribute to the radiative heat transfer mechanisms within combustion facilities. The emissivity of single fuel particles, the emissivity of typical ash materials, and the interaction of single particles with incident radiation were addressed, providing a novel base of experimental data for combustion system simulations.

The received results of fuel particle emissivities extended the previously available data, which mainly consisted of results from non-reacting fuel samples by reacting single particle data. Within this, a decrease of the emissivity with increasing particle conversion and the effect of the mineral content of the fuel on the emissivity has been investigated by experiments with doped fuels. A doping with Fe_2O_3 showed an increased emissivity compared to SiO_2. Single particle emissivity was shown to be temperature dependent, with emissivity decreasing as particle temperature increased.

Addressing the emissivity of ashes, typical ash components as well as their mixtures were investigated spectroscopically. For carbonates and sulphates, the spectral emittance trend is similar and typical for minerals. The emittance is small for low temperatures and increases with wavelength. Characteristic emission bands were identified, caused by CO_3 and the S–O functional groups.

At last, the interaction of radiation with single fuel particles was investigated by determining a representative complex index of refraction. Walnut shell and coal particles have been studied by measuring the scattering phase function, which provides the refractive index by applying an inverse Mie theory approach. While the real and imaginary part of reacting and non-reacting coal are approximately constant, the walnut shell showed a clear increase of both IOR parts with wavelength.

Acknowledgements This work has been funded by the Deutsche Forschungsgemeinschaft (DFG, German Research Foundation)—215035359—SFB/TRR 129 'Oxyflame'.

References

1. Chen, L., Yong, S. Z. and Ghoniem, A. F. "Oxy-Fuel Combustion of Pulverized Coal: Characterization, Fundamentals, Stabilization and CFD Modeling". *Progress in Energy and Combustion Science* 38.2 (2012), 156–214. https://doi.org/10.1016/j.pecs.2011.09.003
2. Boow, J. and Goard, P. R. C. "Fireside Deposits and Their Effect on Heat Transfer in a Pulverized-Fuel-Fired Burner: Part III: The Influence of the Physical Characteristics of the Deposit on its Radiant Emittance and Effective Thermal Conductance". *Journal of the Institute of Fuel* 42 (1969), 412–419.
3. Wall, T. F., Lowe, A., Wibberley, L. J. and McC. Stewart, I. "Mineral Matter in Coal and the Thermal Performance of Large Boilers". *Progress in Energy and Combustion Science* 5.1 (1979), 1–29. https://doi.org/10.1016/0360-1285(79)90017-0
4. Brewster, M. Q. and Kunitomo, T. "The Optical Constants of Coal, Char, and Limestone". *Journal of Heat Transfer* 106.4 (1984), 678–683. https://doi.org/10.1115/1.3246738
5. Greffrath, F., Schiemann, M., Scherer, V. and Gwosdz, A. "Spectral Emittance Characteristics of Powdery and Molten Coal Ashes". *World of Coal Ash Conference*. Denver, Colorado,USA, 2011.
6. Baxter, L. L., Fletcher, T. H. and Ottesen, D. K. "Spectral Emittance Measurements of Coal Particles". *Energy & Fuels* 2 (1988), 423–430. https://doi.org/10.1021/ef00010a007
7. Solomon, P. R., Carangelo, R. M., Best, P. E., Markham, J. R. and Hamblen, D. G. "The Spectral Emittance of Pulverized Coal and Char". *Symposium (International) on Combustion* 21.1 (1988), 437–446. https://doi.org/10.1016/S0082-0784(88)80271-6
8. Solomon, P. R., Chien, P. L., Carangelo, R. M., Best, P. E. and Markham, J. R. "Application of FT-IR Emission/Transmission (E/T) Spectroscopy to Study Coal Combustion Phenomena". *Symposium (International) on Combustion* 22.1 (1989), 211–221. https://doi.org/10.1016/S0082-0784(89)80027-X
9. Bhattacharya, S. and Wall, T. F. "Development of Emittance of Coal Particles During Devolatilisation and Burnoff". *Fuel* 78.5 (1999), 511–519. https://doi.org/10.1016/S0016-2361(98)00178-1
10. Rego-Barcena, S., Saari, R., Mani, R., El-Batroukh, S. and Thomson, M. J. "Real Time, Non-Intrusive Measurement of Particle Emissivity and Gas Temperature in Coal-Fired Power Plants". *Measurement Science and Technology* 18.11 (2007), 3479–3488. https://doi.org/10.1088/0957-0233/18/11/031
11. Bäckström, D., Johansson, R., Andersson, K., Johnsson, F., Clausen, S. and Fateev, A. "Measurement and Modeling of Particle Radiation in Coal Flames". *Energy & Fuels* 28.3 (2014), 2199–2210. https://doi.org/10.1021/ef402271g
12. Yin, C. "On Gas and Particle Radiation in Pulverized Fuel Combustion Furnaces". *Applied Energy* 157 (2015), 554–561. https://doi.org/10.1016/j.apenergy.2015.01.142
13. Graeser, P. and Schiemann, M. "Char Particle Emissivity of Two Coal Chars in Oxy-Fuel Atmospheres". *Fuel* 183 (2016), 405–413. https://doi.org/10.1016/j.fuel.2016.06.116
14. Pörtner, L., Gu, Y. and Schiemann, M. "Investigation of Pulverized Biomass and Coal Char Emissivity". *Energies* 13.18 (2020), 4620. https://doi.org/10.3390/en13184620
15. Graeser, P. and Schiemann, M. "An Attempt to Measure the Emissivity of Burning Coal Particles in Oxy-Fuel Atmospheres: Test Rig Calibration and First Results". *40th International Technical Conference on Clean Coal & Fuel Systems*. Clearwater, Florida, USA, 2015.
16. Graeser, P., Wütscher, A., Cerciello, F., Muhler, M. and Schiemann, M. "Emissivity Comparison Between Chars and Demineralized Coal Chars Under Oxycombustion Conditions". *Chemical Engineering & Technology* 41.7 (2018), 1490–1496. https://doi.org/10.1002/ceat.201700040

17. Graeser, P. and Schiemann, M. “Emissivity of Burning Bituminous Coal Char Particles – Burnout Effects”. *Fuel* 196 (2017), 336–343. https://doi.org/10.1016/j.fuel.2017.01.110
18. Graeser, P. and Schiemann, M. “Corrigendum to “Emissivity of Burning Bituminous Coal Char Particles – Burnout Effects” [Fuel 196 (2017) 336–343] (-)”. *Fuel* 234 (2018), 225–226. https://doi.org/10.1016/j.fuel.2018.07.027
19. Graeser, P., Pörtner, L. and Schiemann, M. “Influence of the Mineral Content on the Emissivity of Hydrothermal Char”. *Chemical Engineering & Technology* 43.5 (2020), 1016–1020. https://doi.org/10.1002/ceat.201900623
20. Greffrath, F., Gorewoda, J., Schiemann, M. and Scherer, V. “Influence of Chemical Composition and Physical Structure on Normal Radiant Emittance Characteristics of Ash Deposits”. *Fuel* 134 (2014), 307–314. https://doi.org/10.1016/j.fuel.2014.05.047
21. Graeser, P. and Schiemann, M. “Investigations on the Emissivity of Burning Coal Char Particles: Influence of Particle Temperature and Composition of Reaction Atmosphere”. *Fuel* 263 (2020), 116714. https://doi.org/10.1016/j.fuel.2019.116714
22. Gorewoda, J. and Scherer, V. “Influence of Carbonate Decomposition on Normal Spectral Radiative Emittance in the Context of Oxyfuel Combustion”. *Energy & Fuels* 30.11 (2016), 9752–9760. https://doi.org/10.1021/acs.energyfuels.6b01398
23. Shimogori, M., Yoshizako, H., Shimogori, Y., Richardson, M. F., Shimogori, M., Yoshizako, H. and Shimogori, Y. “Characterization of Coal Ash Emissivity in High Temperature Atmospheres”. *JSME International Journal Series B* 49.2 (2006), 265–270. https://doi.org/10.1299/jsmeb.49.265
24. Saljnikov, A., Gojak, M., Trifunović, M., Andrejević, S. and Dobrnjac, M. “Research on Infrared Emission Spectra of Pulverized Coal Ash Deposits”. *FME Transactions* 41.1 (2013), 41–48.
25. Wall, T., Bhattacharya, S., Zhang, D. K., Gupta, R. P. and He, X. “The Properties and Thermal Effects of Ash Deposits in Coal-Fired Furnaces”. *Progress in Energy and Combustion Science* 19.6 (1993), 487–504. https://doi.org/10.1016/0360-1285(93)90002-V
26. Markham, J. R., Best, P. E., Solomon, P. R. and Yu, Z. Z. “Measurement of Radiative Properties of Ash and Slag by FT-IR Emission and Reflection Spectroscopy”. *Journal of Heat Transfer* 114.2 (1992), 458–464. https://doi.org/10.1115/1.2911295
27. Shimogori, M., Yoshizako, H. and Matsumura, Y. “Determination of Coal Ash Emissivity Using Simplified Equation for Thermal Design of Coal-Fired Boilers”. *Fuel* 95 (2012), 241–246. https://doi.org/10.1016/j.fuel.2011.11.005
28. Goodwin, D. G. and Mitchner, M. “Infrared Optical Constants of Coal Slags: Dependence on Chemical Composition”. *Journal of Thermophysics and Heat Transfer* 3.1 (1989), 53–60. https://doi.org/10.2514/3.125
29. Gorewoda, J. and Scherer, V. “Normal Radiative Emittance of Coal Ash Sulfates in the Context of Oxyfuel Combustion”. *Energy & Fuels* 31.4 (2017), 4400–4406. https://doi.org/10.1021/acs.energyfuels.6b02866
30. Gorewoda, J., Maas, P. and Scherer, V. “Emittance of Typical Ash Minerals: Influence of Particle Size and Mixtures of Carbonates and Sulfates”. *Energy Procedia* 158 (2019), 1780–1785. https://doi.org/10.1016/j.egypro.2019.01.420
31. Gorewoda, J. “Bestimmung der temperaturabhängigen spektralen Emissionsgrade von Aschen und Aschebestandteilen unter Oxyfuel-Bedingungen”. PhD thesis. Ruhr-Universität Bochum, 2018.
32. Marzo, A., Seah, S. A., Drinkwater, B. W., Sahoo, D. R., Long, B. and Subramanian, S. “Holographic Acoustic Elements for Manipulation of Levitated Objects”. *Nature communications* 6 (2015), 8661. https://doi.org/10.1038/ncomms9661
33. Koch, M., Pielsticker, S., Ströhle, J. and Kneer, R. “Experimental Determination of the Optical Properties of Walnut Shell Particles”. *Journal of Quantitative Spectroscopy and Radiative Transfer* 329 (2024), 109202. https://doi.org/10.1016/j.jqsrt.2024.109202
34. Koch, M., Pörtner, L., Gu, Y., Schiemann, M., Rohlfs, W. and Kneer, R. “Comparison of Scattering Phase Functions of Reacting and Non-Reacting Pulverised Fuel Particles”. *Fuel* 287 (2021), 119415. https://doi.org/10.1016/j.fuel.2020.119415